Ultrasonics 51 (2011) 229–237

Contents lists available at ScienceDirect

Ultrasonics

journal homepage: www.elsevier.com/locate/ultras

A new algorithm for spatial impulse response of rectangular planar transducers

Jiqi Cheng [a], Jian-yu Lu [b], Wei Lin [a], Yi-Xian Qin [a,*]

[a] Department of Biomedical Engineering, Stony Brook University, Stony Brook, NY 11794, USA
[b] Department of Bioengineering, The University of Toledo, Toledo, OH 43606, USA

ARTICLE INFO

Article history:
Received 15 May 2010
Received in revised form 20 August 2010
Accepted 24 August 2010
Available online 4 September 2010

Keywords:
Array transducer
Spatial impulse response
Transient field
Continuous field
Scanning ultrasound

ABSTRACT

Previous solutions for spatial impulse responses of rectangular planar transducers require either approximations or complex geometrical considerations. This paper describes a new, simplified and exact solution using only trigonometric functions and simple set operations. This solution, which can be numerically implemented with a straightforward algorithm, is an exact implementation of the Rayleigh integral without any far field or paraxial approximation. Additionally, a nonlinear relationship was also established for spatial impulse responses from two field points which share the same projection point on the transducer surface plane. By incorporating this relationship in the algorithm, the computational efficiency of spatial impulse responses and continuous fields is improved about 20-folds and 14-folds, respectively. This algorithm has practical applications in designing l-D linear/phased arrays, 1.5-D arrays and 2-D arrays, as demonstrated through numerical simulations with array transducers. Experiments were also conducted to verify the new solution and results show that the algorithm is both accurate and efficient. The application of this method may include development of ultrasound imaging system for hard and soft tissue nondestructive assessment.

1. Introduction

Pulsed excitations are usually employed to generate transient ultrasound fields and to probe the internal structure of objects in ultrasound imaging. Accurate calculation of the transient field emitted from transducers is very important in transducer design and ultrasound system optimization. Harris [1] presented an excellent review on the theories and mathematical methods for transient field calculation. For the rigidly baffled planar sources, the most commonly employed method is the spatial impulse response approach, originally proposed by Tupholme [2] and later by Stepanishen [3,4]. In the classic treatment, the solution for the linear lossless wave equation of velocity potential is expressed as the Rayleigh integral. According to the linear system theory, the integral can be further expressed as the temporal convolution between the driving velocity and the spatial impulse response between the field point and the transducer. At each field point, the spatial impulse response is a function of time. Based on Huygen's principle, the impulse response can be evaluated using intersections between the ultrasound source and a spherical wave, which originates from the field point. Over the years, ultrasound sources of different geometrical shapes, such as circles [3], rectangles [5–7], triangles [8], polygons [9] and curved strips [10] have been studied. In the classic form, the velocity distribution needs to be uniform. To overcome this limitation, Harris [11] and Tjotta and Tjotta [12] suggested generalized impulse response methods to treat nonuniform velocity distribution on the transducer surface. The impulse response approach has also been further developed by Lasota et al. [13] using the line impulse response and by Scarano et al. [14] who expressed impulse response as functions of spatial coordinates instead of time.

The solution for spatial impulse response is highly dependent on the shape of the sources. The solution for the planar circular source is relatively simple, because only one parameter, such as radius, is needed to describe the source. However, rectangular sources require two separate parameters, i.e. width and height, and the solution for the impulse response becomes rather complex due to the discontinuities of the intersections. To simplify the solution, Stepanishen [3] divided the rectangular source into small pieces and applied far field approximations for each small rectangular source, whose response is a trapezoid. The impulse response for the entire source was the summation of the smaller pieces. Lockwood and Willette [5] were the first to derive the exact solution for rectangular sources. They divided the source into four subrectangular sections by projecting the field point to the source surface. The exact expression was given for each subsection, where the projection point is one vertex of the sub-rectangle. The solution for the whole source was finally expressed as the superposition of the four subsections. Without using division and superposition, the exact solution for a rectangular source can be derived by exhaustive geometrical considerations of the relative position of the field

* Corresponding author. Tel.: +1 631 632 1481; fax: +1 631 632 8577.
E-mail address: Yi-Xian.Qin@sunysb.edu (Y.-X. Qin).

0041-624X/$ - see front matter © 2010 Elsevier B.V. All rights reserved.
doi:10.1016/j.ultras.2010.08.007

point to the source. Emeterio and Ullate [7] provided a complete solution after identifying four geometrical areas and a total of 18 different conditions. For numerical implementation, Jensen [8,9] developed a new calculation procedure that sorts angles based on geometrical considerations. All the described approaches require either approximations or complex geometrical considerations. Therefore, a simplified and exact solution is needed.

In this work, a new approach was developed to calculate the spatial impulse response for rectangular transducers. With this approach, the exact solution is derived in terms of the elementary operation of sets and trigonometric functions. Compared to previous solutions, it has several advantages. First, the solution is exact, unlike the solutions provided by Stepanishen [3] and Lee and Benkeser [15], where far field approximation is used. Second, the approach does not involve division and superposition like the exact solution provided by Lockwood and Willette [5]. Third, the approach is straightforward and easy to implement compared to the solutions proposed by Emeterio and Ullate [7] and Jensen [8,9] that involve complex geometrical considerations and angle sorting. Additionally, a new, nonlinear relationship is also established for the spatial impulse responses of two different field points sharing the same projection point on the transducer surface plane. With this nonlinear conversion, the new method and algorithm improve the computational efficiency dramatically in numerical implementation.

The solution and the algorithm developed here have broad applications in the transient/continuous field calculations for 1-D linear/phased arrays, 1.5-D arrays and 2-D arrays, which are essential in ultrasound system simulations and optimizations. To demonstrate such applications, numerical examples of spatial impulse response, transient/continuous fields and transmission/reception system response were provided in the context of a linear array.

2. Theory

As shown in Fig. 1a, a rigidly-baffled rectangular transducer is located on plane $z = 0$, with a height of h and a width of w. The center of the transducer is at the origin of the coordinates. According to the Rayleigh integral [1], the solution to the linear lossless scalar wave equation can be expressed as,

$$\Phi(x,y,z;t) = \int_s \frac{u(t-R/c)}{2\pi R} ds, \tag{1}$$

where $\Phi(x,y,z;t)$ is the velocity potential; R is the distance between transducer element ds and the field point (x,y,z); c is the speed of sound in the media; and $u(t)$ is the uniform velocity distribution normal to the transducer surface. The term $u(t-R/c)$ can be written in the integration form,

$$u(t-R/c) = \int_{-\infty}^{+\infty} u(\tau)\delta(t-R/c-\tau)d\tau. \tag{2}$$

Substituting the above equation into Eq. (1) and changing the order of integration yield,

$$\Phi(x,y,z;t) = \int_{-\infty}^{+\infty} u(\tau) \int_s \frac{\delta(t-R/c-\tau)}{2\pi R} ds d\tau. \tag{3}$$

If a new function is defined as,

$$h(x,y,z;t) = \int_s \frac{\delta(t-R/c)}{2\pi R} ds, \tag{4}$$

then Eq. (3) can be expressed in a convolution form as,

$$\Phi(x,y,z;t) = u(t) * h(x,y,z;t), \tag{5}$$

where $*$ is the convolution in time domain. The function $h(x,y,z;t)$ is also called the spatial impulse response of the system at field point (x,y,z).

The spatial impulse response from Eq. (4) can be expressed explicitly as follows,

$$h(x,y,z;t) = \int_{\Theta_1}^{\Theta_2} \int_{R_1}^{R_2} \frac{\delta(t-R/c)}{2\pi R} r dr d\Theta, \tag{6}$$

Using the relationship $R^2 = r^2 + z^2$ and according to Ref. [9], the above equation can be further simplified as,

$$h(x,y,z;t) = \frac{(\Theta_2 - \Theta_1)c}{2\pi}, \tag{7}$$

where Θ_1 and Θ_2 are determined by the intersection of the transducer and the projected spherical wave with a radius of $R = ct$ (refer to Fig. 1a). The intersection of the spherical wave with the plane $z = 0$ is a circle centered at $(x,y,0)$ with a radius of $r = \sqrt{(ct)^2 - z^2}$ when $t > z/c$. When the circle intersects the transducer aperture, some intersected arcs are located inside the transducer aperture. The angles expanded by these arcs are directly related to the spatial impulse response given by Eq. (7). When more than one arc exists, the spatial impulse response is the summation of contributions from all arcs, and Eq. (7) is changed to the following summation:

$$h(x,y,z;t) = \sum_l \frac{\left(\Theta_2^l - \Theta_1^l\right)c}{2\pi}, \tag{8}$$

where l is the index of the arcs.

To calculate Θ_1 and Θ_2, we shift the origin of the coordinates to $(x,y,0)$ and obtain a new coordinate (x',y',z) as shown in Fig. 1b. With the new 2-D coordinates at the plane $z = 0$, the circle can be expressed in polar coordinates as

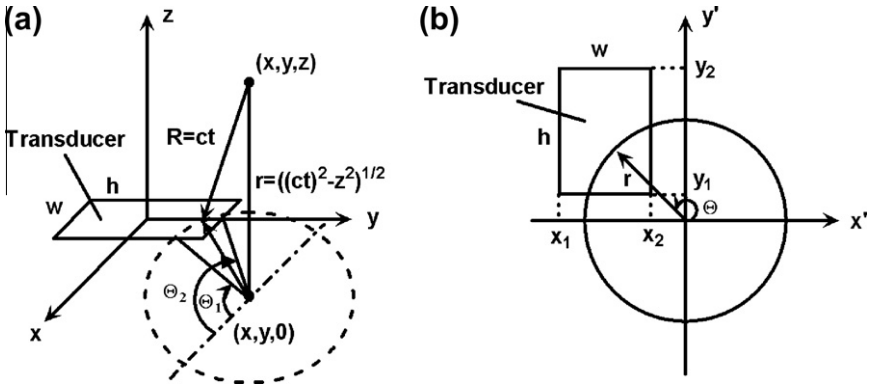

Fig. 1. Geometry of the transducer and the filed point: (a) spherical intersection in original 3-D rectangular coordinates and (b) spherical intersection in the shifted 2-D coordinates.

$$\begin{cases} x' = r\cos\Theta, \\ y' = r\sin\Theta. \end{cases} \tag{9}$$

If a point on the circle is inside the transducer aperture, the angle Θ must satisfy the following inequalities,

$$\begin{cases} x_1 \leqslant r\cos\Theta \leqslant x_2, & \text{(a)} \\ y_1 \leqslant r\sin\Theta \leqslant y_2, & \text{(b)} \end{cases} \tag{10}$$

where x_1, x_2, y_1 and y_2 are the coordinates of the four boundaries of the transducer in the new coordinates given by $x_1 = -x - w/2$, $x_2 = -x + w/2$, $y_1 = -y - h/2$ and $y_2 = -y + h/2$, respectively.

Assuming that Eq. (10a) holds when $\Theta \in \bigcup_i [\Theta^i_{a1}, \Theta^i_{a2}]$ and Eq. (10b) also holds when $\Theta \in \bigcup_j [\Theta^j_{b1}, \Theta^j_{b2}]$, we define the following relation,

$$\bigcup_l \left[\Theta^l_1, \Theta^l_2\right] = \left(\bigcup_i \left[\Theta^i_{a1}, \Theta^i_{a2}\right]\right) \bigcap \left(\bigcup_j \left[\Theta^j_{b1}, \Theta^j_{b2}\right]\right), \tag{11}$$

where i is the index of the sets that satisfy Eq. (10a); j is the index of the sets that satisfy Eq. (10b); $\bigcup$ is the union of the sets; $\bigcap$ is the intersection of the sets; and each set corresponds to an arc. When $\Theta \in \bigcup_l \left[\Theta^l_1, \Theta^l_2\right]$, Eq. (10) is satisfied. With the sets obtained from Eq. (11), the spatial impulse response can be evaluated from Eq. (8).

Calculation of these sets is a matter of trivial algebraic operations involving only elementary trigonometric functions. Notice that Θ is defined on $[0, 2\pi]$, but the inverse cosine and inverse sine functions are defined on different ranges. For example, assuming that the inverse cosine function $\cos^{-1}(x)$ is defined on $[0, \pi]$, from Eq. (10a) we have,

$$\begin{cases} \Theta \in [0,0], \text{ when } \frac{x_1}{r} > 1 \text{ or } \frac{x_2}{r} < -1; \\ \Theta \in \left[\cos^{-1}\left(\frac{x_2}{r}\right), \cos^{-1}\left(\frac{x_1}{r}\right)\right] \bigcup \left[2\pi - \cos^{-1}\left(\frac{x_1}{r}\right), 2\pi - \cos^{-1}\left(\frac{x_2}{r}\right)\right], \\ \quad \text{when } \frac{x_1}{r} \geqslant -1 \text{ and } \frac{x_2}{r} \leqslant 1; \\ \Theta \in \left[\cos^{-1}\left(\frac{x_2}{r}\right), 2\pi - \cos^{-1}\left(\frac{x_2}{r}\right)\right], \\ \quad \text{when } \frac{x_1}{r} < -1 \text{ and } -1 \leqslant \frac{x_2}{r} \leqslant 1; \\ \Theta \in \left[0, \cos^{-1}\left(\frac{x_1}{r}\right)\right] \bigcup \left[2\pi - \cos^{-1}\left(\frac{x_1}{r}\right), 2\pi\right], \\ \quad \text{when } -1 \leqslant \frac{x_1}{r} \leqslant 1 \text{ and } \frac{x_2}{r} > 1; \\ \Theta \in [0, 2\pi], \text{ when } \frac{x_1}{r} \leqslant -1 \text{ and } \frac{x_2}{r} \geqslant 1. \end{cases} \tag{12}$$

Assuming that the inverse sine function $\sin^{-1}(x)$ is defined on $[-\pi/2, \pi/2]$, from Eq. (10b) we have,

$$\begin{cases} \Theta \in [0,0], \text{ when } \frac{y_1}{r} > 1 \text{ or } \frac{y_2}{r} < -1; \\ \Theta \in \left[\sin^{-1}\left(\frac{y_1}{r}\right), \sin^{-1}\left(\frac{y_2}{r}\right)\right] \bigcup \left[\pi - \sin^{-1}\left(\frac{y_2}{r}\right), \pi - \sin^{-1}\left(\frac{y_1}{r}\right)\right], \\ \quad \text{when } \frac{y_1}{r} \geqslant 0 \text{ and } \frac{y_2}{r} \leqslant 1; \\ \Theta \in \left[\pi - \sin^{-1}\left(\frac{y_2}{r}\right), \pi - \sin^{-1}\left(\frac{y_1}{r}\right)\right] \\ \quad \bigcup \left[2\pi + \sin^{-1}\left(\frac{y_1}{r}\right), 2\pi + \sin^{-1}\left(\frac{y_2}{r}\right)\right], \\ \quad \text{when } \frac{y_1}{r} \geqslant -1 \text{ and } \frac{y_2}{r} \leqslant 0; \\ \Theta \in \left[0, \sin^{-1}\left(\frac{y_2}{r}\right)\right] \bigcup \left[\pi - \sin^{-1}\left(\frac{y_2}{r}\right), \pi - \sin^{-1}\left(\frac{y_1}{r}\right)\right] \\ \quad \bigcup \left[2\pi + \sin^{-1}\left(\frac{y_1}{r}\right), 2\pi\right], \\ \quad \text{when } -1 \leqslant \frac{y_1}{r} \leqslant 0 \text{ and } 0 \leqslant \frac{y_2}{r} \leqslant 1; \\ \Theta \in \left[0, \sin^{-1}\left(\frac{y_2}{r}\right)\right] \bigcup \left[\pi - \sin^{-1}\left(\frac{y_2}{r}\right), 2\pi\right], \\ \quad \text{when } \frac{y_1}{r} < -1 \text{ and } 0 \leqslant \frac{y_2}{r} \leqslant 1; \\ \Theta \in \left[\pi - \sin^{-1}\left(\frac{y_2}{r}\right), 2\pi + \sin^{-1}\left(\frac{y_2}{r}\right)\right], \\ \quad \text{when } \frac{y_1}{r} < -1 \text{ and } -1 \leqslant \frac{y_2}{r} < 0; \\ \Theta \in \left[\sin^{-1}\left(\frac{y_1}{r}\right), \pi - \sin^{-1}\left(\frac{y_1}{r}\right)\right], \\ \quad \text{when } 0 \leqslant \frac{y_1}{r} \leqslant 1 \text{ and } \frac{y_2}{r} > 1; \\ \Theta \in \left[0, \pi - \sin^{-1}\left(\frac{y_1}{r}\right)\right] \bigcup \left[2\pi + \sin^{-1}\left(\frac{y_1}{r}\right), 2\pi\right], \\ \quad \text{when } -1 \leqslant \frac{y_1}{r} < 0 \text{ and } \frac{y_2}{r} > 1; \\ \Theta \in [0, 2\pi], \text{ when } \frac{y_1}{r} \leqslant -1 \text{ and } \frac{y_2}{r} \geqslant 1. \end{cases} \tag{13}$$

The algorithm to calculate the spatial impulse response $h(x, y, z; t)$ for field point (x, y, z) at time t is as follows:

(a) Decide if time t falls into the range in which the impulse response is not zero. The range is defined by $t_{\min} = z/c$ when the spherical wave first intersects the source plane and $t_{\max} = \max\{\sqrt{z^2 + (x \pm w/2)^2 + (y \pm h/2)^2}/c\}$ when the spherical wave interacts the farthest vertex of the rectangular source. If t falls into the range $[t_{\min}, t_{\max}]$, proceed to step (b). Otherwise, the impulse response is zero.

(b) Calculate the radius $r = \sqrt{(ct)^2 - z^2}$ and the shifted coordinates $x_1 = -x - w/2$ and $x_2 = -x + w/2$. Find the union of the sets according to Eq. (12).

(c) Calculate the shifted coordinates $y_1 = -y - h/2$ and $y_2 = -y + h/2$. Find the union of the sets according to Eq. (13).

(d) Calculate the intersections of the unions obtained from step (b) and step (c) according to Eq. (11).

(e) Evaluate the spatial impulse response from the intersections according to Eq. (8).

After the spatial impulse response is evaluated, the pressure at the field point (x, y, z) can be calculated directly as [1],

$$p(x, y, z; t) = \rho_0 \frac{\partial \Phi(x, y, z; t)}{\partial t} = \rho_0 h(x, y, z; t) * \frac{du(t)}{dt}, \tag{14}$$

where ρ_0 is the density of the media.

From the algorithm and Eqs. (8)–(13), it is obvious that the spatial impulse response $h(x, y, z; t)$ depends on the shifted coordinates x_1, x_2, y_1, y_2 and the radius r. If the two coordinates, x and y, of the field points are fixed, spatial impulse response would only depend on radius r. For two field points (x, y, z_0) and (x, y, z_1), if $r_0 = \sqrt{(ct_0)^2 - z_0^2}$ equals to $r_1 = \sqrt{(ct_1)^2 - z_1^2}$, the spatial impulse responses at the two field points are equal for these specific moments and distances, i.e. $h(x, y, z_0; t_0) = h(x, y, z_1; t_1)$. From

$$\sqrt{(ct_0)^2 - z_0^2} = \sqrt{(ct_1)^2 - z_1^2}, \tag{15}$$

we have

$$t_0 = \sqrt{t_1^2 - z_1^2/c^2 + z_0^2/c^2}, \tag{16}$$

where $t_0 \geqslant z_0/c$ and $t_1 \geqslant z_1/c$. Thus we have the following relationship,

$$h(x, y, z_1; t_1) = h\left(x, y, z_0; \sqrt{t_1^2 - z_1^2/c^2 + z_0^2/c^2}\right). \tag{17}$$

If z_0 is set to zero, we get the following after changing the variables:

$$h(x, y, z; t) = h\left(x, y, 0; \sqrt{t^2 - z^2/c^2}\right). \tag{18}$$

Eq. (18) has an important implication for numerical calculation of the spatial impulse response. It means that the spatial impulse response at one field point can be directly related to the response at another point, which is the projection at the transducer surface plane. We only need to calculate the spatial impulse response $h(x, y, 0; t)$ at $(x, y, 0)$ once and save it as a lookup table. The spatial impulse response $h(x, y, z; t)$ at field point (x, y, z) can be evaluated as $h\left(x, y, 0; \sqrt{t^2 - z^2/c^2}\right)$ with one simple nonlinear conversion of time t. For applications where time is evenly sampled, we are attempting to evaluate $h(x, y, z; n\Delta T_2)$ from $h(x, y, 0; m\Delta T_1)$, where ΔT_1 and ΔT_2 are the sampling intervals for $h(x, y, 0; t)$ and $h(x, y, z; t)$ respectively and m and n are natural integers. After nonlinear conversion, we have

$$m\Delta T_1 \leqslant \sqrt{(n\Delta T_2)^2 - z^2/c^2} \leqslant (m+1)\Delta T_1. \tag{19}$$

The converted time $\sqrt{(n\Delta T_2)^2 - z^2/c^2}$ may not exactly fall on the sampled time point. Linear interpolation is needed, and we get

$$h(x,y,z;n\Delta T_2) = \left(m+1-\sqrt{(n\Delta T_2)^2 - z^2/c^2}/\Delta T_1\right)h(x,y,0;m\Delta T_1) + \left(\sqrt{(n\Delta T_2)^2 - z^2/c^2}/\Delta T_1 - m\right)h(x,y,0;(m+1)\Delta T_1). \quad (20)$$

To reduce the numerical error introduced by the interpolation, a smaller sampling interval ΔT_1 can be used to generate the lookup table, which needs to be calculated only once.

3. Results

In this section, applications of the algorithm are demonstrated through numerical simulations and experimental validations. The spatial impulse responses, transient fields, continuous fields and echo signals were calculated for a linear array transducer. The applications for 1.5-D or 2-D arrays can be easily formulated following the same procedure. Experiments were carried out to verify the simulation results of the echo signals. The influences of sampling rate, computational efficiency and accuracy were also addressed.

3.1. Simulation conditions

For numerical simulations, we assumed a linear array transducer with 128 elements. It has a pitch of 0.15 mm, physical dimensions of 19.2 mm × 14 mm, and a central frequency of 2.5 MHz. It models a commercial V2 array transducer from Acuson that was used in the experimental setup. There is no focusing in elevation for numerical simulations while the physical transducer does have one with a focal distance of 68 mm.

For simplicity, the transfer function of the transducer in the simulation was assumed to be a Blackman window for both transmission and reception,

$$B(f) = \begin{cases} 0.42 - 0.5\cos(\pi f/f_c) + 0.08\cos(2\pi f/f_c), & \text{if } 0 \leqslant f \leqslant 2f_c, \\ 0, & \text{if } f > 2f_c. \end{cases} \quad (21)$$

The two-way fractional bandwidth of this function is 64% of the central frequency at −6 dB and the bandwidth of the physical transducer V2 is about 50–60%.

The driving signal for each element in the transient field and echo simulation was a one-cycle sine wave at 2.5 MHz without any time delay, which was also used in the experiments. For continuous field simulation, the driving signal at each element was a continuous sine wave at 2.5 MHz with an initial phase of zero. The weighting level for every element in both simulation and experiment was set to be one and the unit of measurement for the coordinates defined in the following subsections is mm.

The algorithm developed in this study and the classic method developed by Lockwood and Willette [5], which was used as a standard for comparison, were both implemented using C language. The algorithms were tested under the Linux operating system on a PC equipped with dual processors running at 2.8 GHz and a total internal memory of 2 GB.

For numerical error calculation, two paired signals were first normalized separately. Then, the error signal was defined as the absolute difference between the two normalized signals. The maximum error was detected by scanning the error signal from beginning to the end. When two images with multiple paired signals were compared, the overall maximum error across all pairs was obtained by finding the maximum of the maximum errors of each pair. The maximum error is expressed as a percentage.

3.2. Impulse response for array transducer

For a linear array consisting of N flat transducer elements, the impulse response of the whole transducer can be treated as the summation of the individual impulse responses from each element if the same driving signal is applied all elements.

As shown in Fig. 2, the spatial impulse response of the whole transducer for a linear array can be expressed as

$$h(x,y,z;t) = \sum_{i=0}^{N-1} a_i h_i(x,y,z;t), \quad (22)$$

where $h(x,y,z;t)$ is the spatial impulse response of the whole transducer; $i = 0, 1, \ldots, N-1$, is the index of the elements of the array; a_i is the weighting level at element i; $h_i(x,y,z;t)$ is the spatial impulse response between the element i and the field point (x,y,z), which can be calculated according to Eq. (8). However, Eq. (8) only applies when the center of the transducer is located at the origin. Therefore, the origin of the coordinates needs to be shifted to the center of each element and the coordinates of the field point need to be changed accordingly.

The spatial impulse responses of the linear transducer defined in Section 3.1 were calculated. The field points were on two typical lines defined by $(0,0,z)$ and $(20,0,z)$ (refer to Fig. 2 for the definition of the coordinates). One of the lines $(0,0,z)$ has a projection point $(0,0,0)$ that lies inside the transducer aperture, while the projection point $(20,0,0)$ from the other line is outside the transducer aperture.

Fig. 3 shows selected plots of normalized spatial impulse responses at different distances along the line defined by $(0,0,z)$. For clarity, the responses at different distances were vertically shifted in a progressive manner. In reality, all these responses share the same base line of zero. The plots in dashed lines were calculated according to the new algorithm with the nonlinear conversion defined in Eq. (18). The plots in solid lines were calculated directly according to the classic method by Lockwood and Willette [5]. Following the same format, Fig. 4 shows plots of spatial impulse responses along another line defined by $(20,0,z)$.

The spatial impulse responses along these two lines have very distinct features. If a line has a projection point inside the transducer aperture, the spatial impulse responses along the line jump suddenly from zero to their maxima. On the other hand, if the line has a projection point lying outside of the transducer aperture, the spatial impulse responses gradually increase to their maxima. However, the spatial impulse responses for field points along the same line share the same basic characteristics. When a point is further away from the transducer, the main features of the impulse

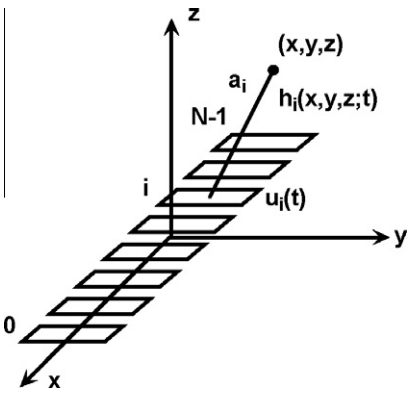

Fig. 2. The geometry of the array transducer and field point.

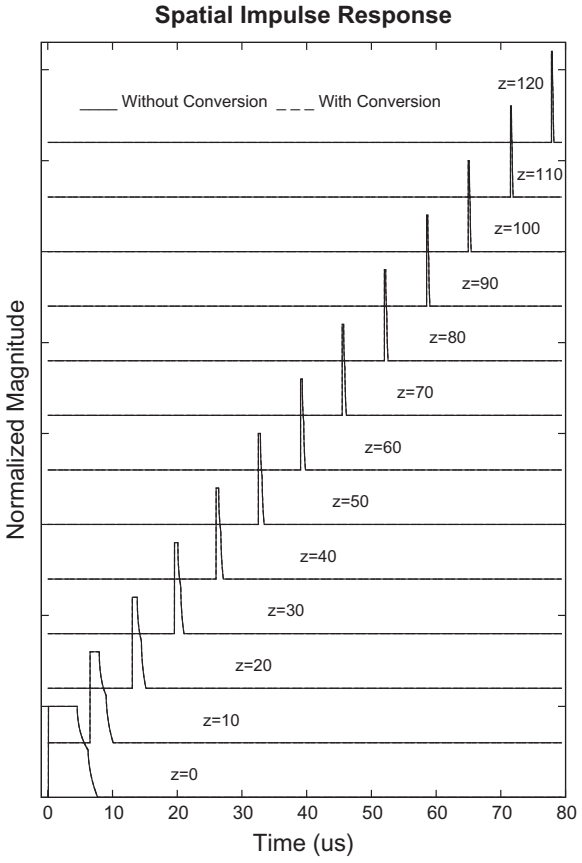

Fig. 3. The plots of the spatial impulse response along line $(0, 0, z)$ with the unit being mm.

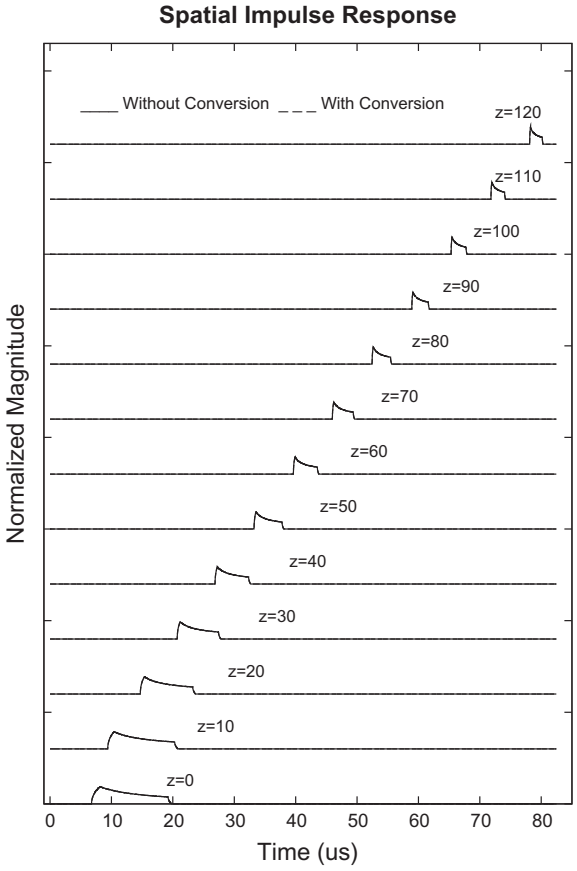

Fig. 4. The plots of the spatial impulse response along line $(20, 0, z)$ with the unit being mm.

response are condensed in time, and the duration is reduced. This phenomenon is predicted by Eq. (18) and is the base for nonlinear conversion. These characteristics of the impulse response have some influence on numerical implementations. When field points further away from the transducer surface are considered, a higher temporal sampling rate is required to meet the sampling requirement and avoid aliases.

For Fig. 3, the spatial impulse responses of 800 field points along the line $(0, 0, z)$ were calculated with a sampling distance of 0.15 mm. It took 15.64 s for the new algorithm and 318.42 s for the classic method. There is a 20-fold increase in calculation speed. For the field points along line $(20, 0, z)$, similar speed improvement was observed. From these selected plots in both Figs. 3 and 4, it is difficult to tell the difference in the results calculated from the different algorithms. However, the numerical implementation of the nonlinear conversion introduced some error to the spatial impulse responses when compared to the responses calculated directly with the classic method, which is exact at specific sampling frequency. With a temporal sampling frequency of 100 MHz, the maximum errors across all the field points were 1.55% and 2.40% for the lines $(0, 0, z)$ and $(20, 0, z)$ respectively.

3.3. Transient field calculation for array transducer

To calculate the transient field at point (x, y, z) for a linear array transducer, one can add the pressure from each element (as defined in Eq. (14)) together as follows,

$$p(x, y, z; t) = \rho_0 \sum_{i=0}^{N-1} a_i h_i(x, y, z; t) * \frac{\partial u_i(t)}{\partial t}, \tag{23}$$

where $u_i(t)$ is the velocity profile for element i, and all the other parameters have the same definitions as those in Eq. (22). Here, the velocity profile of each element does not have to be the same. For example, to generate a focused pulse, a different time delay is needed for each element, and the velocity profile $u_i(t)$ has to be different for every element.

Fig. 5 shows the transient fields for four selected points at $(0, 0, 60)$, $(6, 0, 60)$, $(0, 0, 120)$ and $(6, 0, 120)$. A pulsed plane wave was simulated, and the transmit transfer function defined by Eq. (21) was also included and acted as a band pass filter for the excitation signal. The time duration of these transient fields was truncated to a window of 5 μs with the starting moment shifted to show details of the wave.

The temporal sampling frequency has a major influence on the numerical accuracy of the transient fields calculated using all spatial impulse response approaches. The study conducted by Crombie et al. [16] showed that the maximum error is about 5% at a sampling rate of 250 MHz for exact solutions. The errors were calculated by comparing the fields to those calculated with a sampling rate of 4 GHz. For the linear array defined here, the maximum errors of the transient fields are calculated for 128 field points with a spatial sampling distance of 0.15 mm on a line defined by $(x, 0, 120)$. At sampling frequencies of 40 MHz, 160 MHz, 320 MHz and 640 MHz, the maximum errors are 13.7%, 2.67%, 1.14% and 0.69%, respectively. These errors were calculated using the transient field at 5120 MHz as the standard for comparison, since an even higher sampling rate would not significantly improve accuracy. The base frequency of 40 MHz was chosen because it was the sampling frequency used in the experiment. Considering the different transducer configurations involved, the results agree with

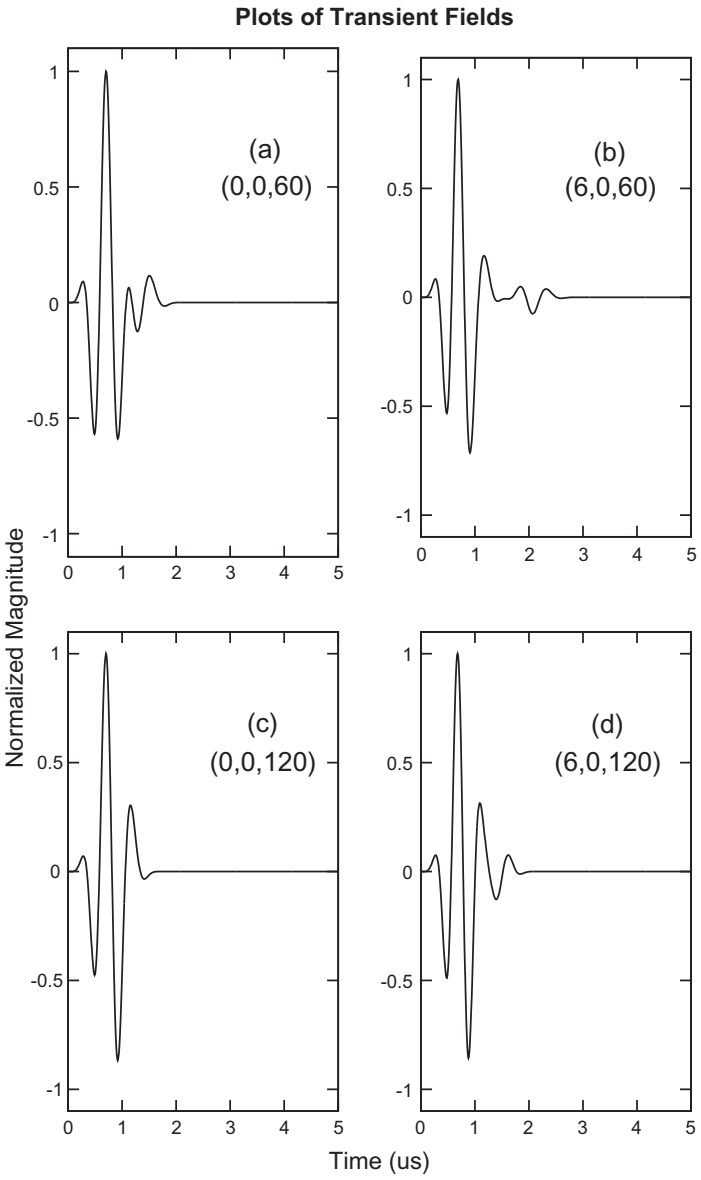

Fig. 5. The plots of transient fields at four points: (a) (0, 0, 60), (b) (6, 0, 60), (c) (0, 0, 120) and (d) (6, 0, 120) with the unit being mm.

those in literature. For the field point (x, y, z) with a projection point lying inside the transducer aperture, the spatial impulse response jumps suddenly from zero to maximum at the moment $t = z/c$ as shown in Fig. 3. Theoretically, the sampling frequency has to be infinite to capture the sudden jump at the precise moment. When finite sampling frequency is used, the starting moment of the spatial impulse response always has an uncertainty of ΔT, which is the temporal sampling interval. If the transient field shape, not the starting moment, is the major concern, the uncertainty can be partially corrected by shifting the starting moment within ΔT. With the correction, the maximum errors at 40 MHz, 160 MHz, 320 MHz and 640 MHz drop significantly to 3.90%, 0.98%, 0.43%, and 0.30% respectively, which implies that the sampling rate does not have to be extremely high to have acceptable accuracy in terms of the shape of the transient field.

3.4. Continuous field calculation for array transducer

The continuous field is a special case of transient fields, where the excitation is a continuous harmonic wave instead of a pulse. Referring to Eq. (14), if $u(t) = e^{j(\omega_0 t+\phi)}$, we have

$$p(x,y,z;t) = \rho_0 h(x,y,z;t) * de^{j(\omega_0 t+\phi)}/dt, \tag{24}$$

where ω_0 and ϕ are the angular frequency and initial phase of the driving signal respectively. Eq. (24) can be explicitly rewritten as

$$p(x,y,z;t) = j\omega_0\rho_0 \int_{-\infty}^{+\infty} h(x,y,z;\tau)e^{-j\omega_0\tau}d\tau e^{j(\omega_0 t+\phi)}. \tag{25}$$

Defining the time domain Fourier transform of $h(x, y, z; t)$ as

$$H(x,y,z;\omega) = \int_{-\infty}^{+\infty} h(x,y,z;\tau)e^{-j\omega\tau}d\tau, \tag{26}$$

Eq. (25) can be simplified as follows,

$$p(x,y,z;t) = j\omega_0\rho_0 H(x,y,z;\omega_0)e^{j(\omega_0 t+\phi)}. \tag{27}$$

For array transducer, if every element is driven at the same frequency ω_0; from Eq. (23) and Eq. (27), we obtain

$$p(x,y,z;t) = j\omega_0\rho_0 e^{j\omega_0 t}\sum_{i=0}^{N-1} a_i H_i(x,y,z;\omega_0)e^{j\phi_i}, \tag{28}$$

where $H_i(x, y, z; \omega_0)$ is the Fourier transform of $h_i(x, y, z; t)$ evaluated at frequency ω_0, and ϕ_i is the initial phase of the driving signal at

element i. When the initial phases of each element are the same, a continuous plane wave can be obtained. For a continuous focused wave, the initial phases at different elements need to be different.

The continuous plane-wave fields at central frequency of 2.5 MHz for the array transducer were calculated and displayed in Fig. 6. The amplitude of the fields was normalized and log-compressed to −40 dB. The field points are located on the plane defined by $(x, 0, z)$ with dimensions of 38.4 mm by 120 mm. The spatial sampling distance is 0.15 mm in each direction. The field in panel (a) is calculated using the method developed in this study with nonlinear conversion, while the one in panel (b) is evaluated directly using the classic method. It took 52.5 min and 746.2 min to calculate panel (a) and panel (b) respectively at a temporal sampling frequency of 100 MHz. In terms of the computational efficiency, an improvement of 14-folds is achieved with the new method. The nonlinear conversion only introduces a negligible maximum error of 0.49% across all field points.

For continuous field calculation, the spatial impulse response approach has a unique feature. As seen in Eqs. (24)–(28), one has to calculate the time-domain spatial impulse response, which is the most time-consuming part, before calculating the continuous field at one specific frequency. The next step is to obtain the Fourier transform of these responses. With fast Fourier transform, the continuous fields at all frequencies, which are smaller than half of the sampling frequency, are calculated at the same time. This allows the continuous fields at all frequencies to be evaluated without further calculations. In addition, this approach can calculate the continuous field starting right from the transducer surface unlike the classic Rayleigh–Sommerfeld method [17] which is unable to do so because it needs numerical double integration. When the field point gets too close to the source, the phases change too rapidly for the integration to converge. To overcome the limitation of the Rayleigh–Sommerfeld method, the distribute point source method (DPSM) [18–20] was recently proposed. This method uses distributed point sources located slightly behind the transducer surface to model the transducer. In this way, the continuous field that starts right from the transducer surface can be calculated by summing the contribution from all point sources, whose strengths are determined by the boundary condition on the transducer surface. Detailed comparisons between DPSM and our approach are beyond the scope of this paper. Therefore, only a brief comparison will be made here. When implemented under the same conditions as described in Section 3.1, DSPM took 8.1 min and 32.4 min to calculate the same field when 128×93 and 256×186 point sources of uniform strength were used, respectively. These fields are displayed in Fig. 7. The maximum errors of these two fields compared to the field calculated with the classic method (as displayed in Fig. 6b), are 20.48% and 11.62%, respectively. The maximum error decreases when the density of the point sources increases, however these errors are all significantly higher than the error from our method (as displayed in Fig. 6a), which is 0.49%. It is obvious that the density of the distributed point sources for DPSM has to be increased to improve accuracy, which in turn, would increase calculation time dramatically. On the other hand, the calculation time of our method was reduced to only 5.2 min when one single large-aperture transducer, instead of the 128-element array transducer, was assumed in implementation. Take note that the errors for DPSM are noticeably higher than those described in Ref. [20]. This could possibly be due to the fact that off-axis field points were included in this work and different comparison criteria were used.

3.5. Echo simulation and experiment for array transducer

Based on the linear system theory [16,21], the pulse-echo response of a linear array transducer can be easily modeled. When one point at (x, y, z) (refer to Fig. 2) is insonifed by ultrasound, it scatters the ultrasound with a coefficient $f(x, y, z)$. Then the scattered ultrasound received by an element of the array transducer is given by [21],

$$p_i^r(x,y,z;t) = \frac{\rho_0}{c} f(x,y,z) h_i(x,y,z;t) * \left[\sum_{i=0}^{N-1} a_i h_i(x,y,z;t) * \frac{d^2 u_i(t)}{d^2 t} \right]. \quad (29)$$

If the electro-mechanical transfer function of the array is $B(t)$, then the electrically received echo signal from element i can be expressed as,

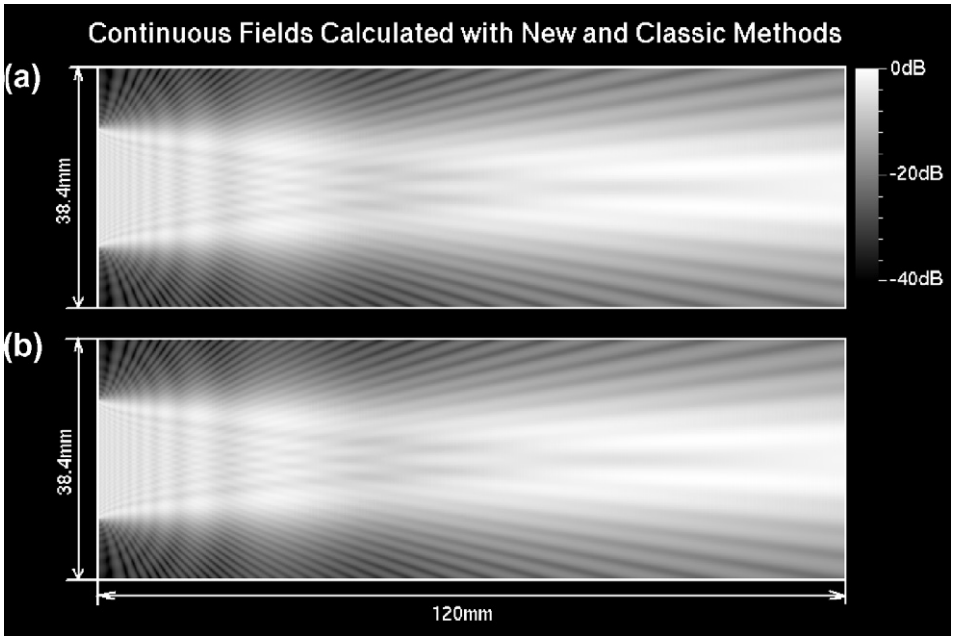

Fig. 6. Continuous plane-wave fields for the array transducer at 2.5 MHz: (a) new method and (b) classic method.

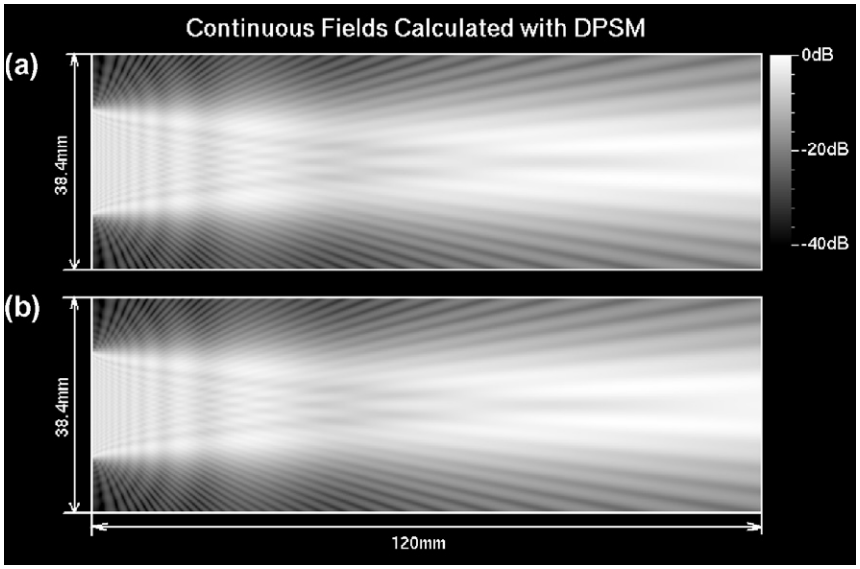

Fig. 7. Continuous plane-wave fields for the array transducer at 2.5 MHz: (a) DPSM with 128 × 93 point sources and (b) DPSM with 256 × 186 point sources.

$$e_i(t) = \frac{\rho_0}{c} f(x,y,z)B(t) * h_i(x,y,z;t) * \left[\sum_{i=0}^{N-1} a_i h_i(x,y,z;t) * \frac{d^2 u_i(t)}{d^2 t}\right]. \quad (30)$$

When weak scattering approximation or First Born approximation [22] is assumed, one obtains the echo signals from multiple scattering points as the summation of the contributions from each point as defined in Eq. (30).

Echo signals were simulated and experimentally collected for four separate points with coordinates of (0, 0, 30), (0, 0, 50), (0, 0, 70) and (0, 0, 90) respectively. The experiment was conducted in degassed water at room temperature and a small glass ball with a diameter of 0.5 mm served as a point scatterer. The scatterer was placed at the center of the transducer and vertically descended to an appropriate depth using a stepping motor. The depth was also independently verified by the time of flight of the echoes. The echo data was digitized with a resolution of 12 bits and a sampling frequency of 40 MHz by a self-built ultrasound imaging system [23] that has 128 independent transmit/receive channels.

Fig. 8 shows the echo signals with time duration of 5 μs. The echo signals detected by all 128 elements were converted to grey scale and arranged in parallel to form a 2D image. The horizontal dimension for these images is time, while the vertical dimension is the index of each element, starting from 0 to 127. Fig. 9 shows the line plots of the normalized echoes at element 64. The simulated echo signals are displayed in solid lines and the experimental ones in dashed lines.

From these two figures, one can observe that the simulation agrees with the experiment fairly well. The main features of the

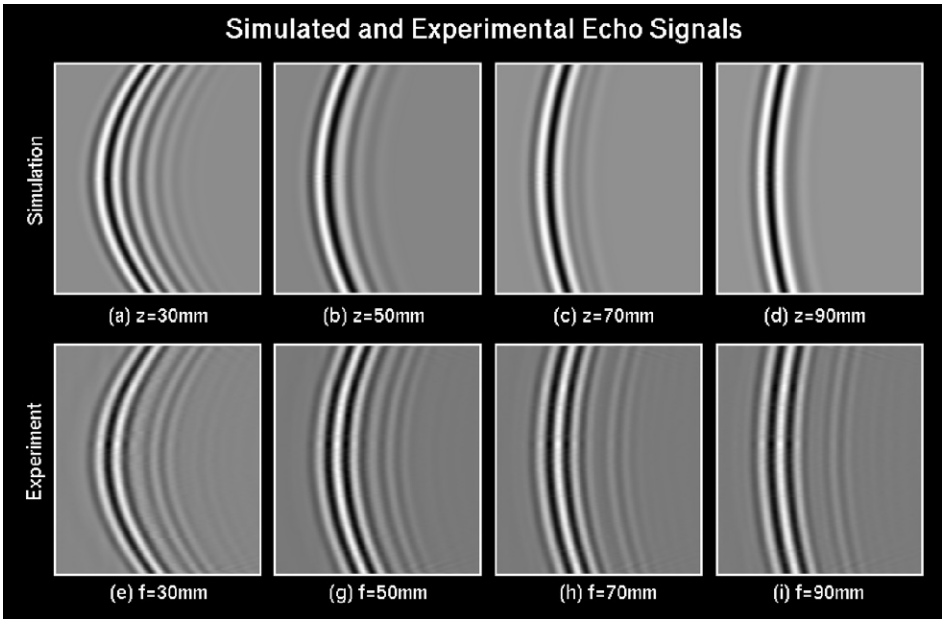

Fig. 8. Simulated and experimental echo signals: (a–d) are simulated results for four points at the center of the transducer with a distance of 30 mm, 50 mm, 70 mm and 90 mm away from the transducer surface respectively. (e–i) are experimental results in water for the same points as in (a–d). The vertical dimension is the index of elements of the transducer, and the horizontal dimension is time.

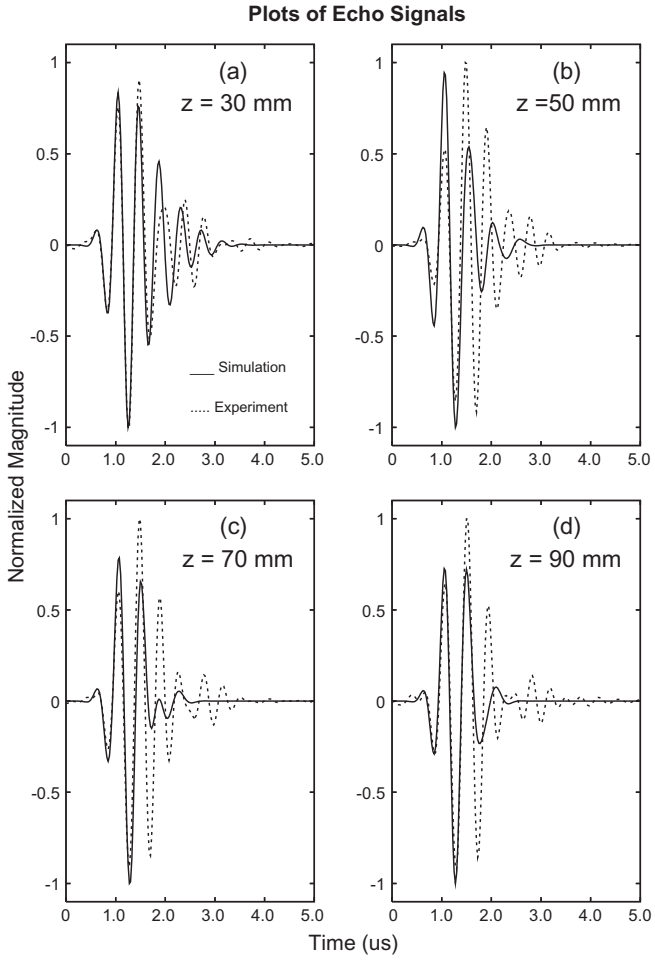

Fig. 9. The plots of echo signals at element 64 as in Fig. 8: (a) $z = 30$ mm, (b) $z = 50$ mm, (c) $z = 70$ mm and (d) $z = 90$ mm.

echoes from the simulation were very similar to those from the experiment. However, some differences do exist. For example, the echoes in the experiment last longer than those in the simulation. There are several possible causes for such differences. First, the transfer function used in the simulation was the well-defined Blackman window whose two-way bandwidth is slightly higher than that of the physical V2 transducer, resulting in a shorter pulse. Second, an ideal point scatterer was assumed in the simulation, while a glass ball with a diameter close to the central wavelength of the transducer was used in the experiment. Third, there is a physical focus at 68 mm in elevation for the V2 transducer while no focusing in elevation was assumed in simulation.

4. Conclusion

Spatial impulse response method is very important for transient, continuous field calculations and transducer designs. The previous solutions of the spatial impulse response for rectangular planar transducers required divisions and superposition, complicated geometrical considerations or far field approximations. In this study, we developed a simple and exact solution involving only elementary trigonometric functions and simple set operations. A nonlinear relationship was also established for the spatial impulse responses from two field points sharing the same projection point in the transducer surface plane. Coupled with this nonlinear conversion, the new method achieved a 20-fold and 14-fold increase in computational efficiency for spatial impulse response calculation and continuous field calculation respectively. This method may have potential to improve the design of ultrasound imaging system for hard and soft tissue nondestructive assessment.

Acknowledgements

This work is kindly supported by the National Space Biomedical Research Institute through NASA Cooperative Agreement NCC 9-58, the NIH (AR52379), and US Army Medical Research. The authors are also grateful to Mr. Alain Rivolle, Professor Dominique Placko and Professor Tribikram Kundu for their help on the DPSM.

References

[1] G.R. Harris, Review of transient field theory for a baffled planar piston, J. Acoust. Soc. Am. 70 (1981) 10–20.
[2] G.E. Tupholme, Generation of acoustic pulses by baffled plane pistons, Mathematika 16 (1969) 209–224.
[3] P.R. Stepanishen, Transient radiation from pistons in an infinite planar baffle, J. Acoust. Soc. Am. 49 (1971) 1629–1638.
[4] P.R. Stepanishen, The time-dependent force and radiation impedance on a piston in a rigid infinite planar baffle, J. Acoust. Soc. Am. 49 (1971) 841–849.
[5] J.C. Lockwood, J.G. Willette, High-speed method for computing the exact solution for the pressure variations in the nearfield of a baffled piston, J. Acoust. Soc. Am. 53 (1973) 735–741.
[6] L.G. Ullate, J.L.S. Emeterio, A new algorithm to calculate the transient near-field of ultrasonic phased arrays, IEEE Trans. Ultrason. Ferroelect. Freq. Control 39 (1992) 745–753.
[7] J.L.S. Emeterio, L.G. Ullate, Diffraction impulse response of rectangular transducers, J. Acoust. Soc. Am. 92 (1992) 651–662.
[8] J.A. Jensen, Ultrasound fields from triangular apertures, J. Acoust. Soc. Am. 100 (1996) 2049–2056.
[9] J.A. Jensen, A new calculation procedure for spatial impulse responses in ultrasound, J. Acoust. Soc. Am. 105 (1999) 3266–3274.
[10] P. Faure, D. Cathignol, J.Y. Chapelon, V.L. Newhouse, On the pressure field of a transducer in the form of a curved strip, J. Acoust. Soc. Am. 95 (1994) 628–637.
[11] G.R. Harris, Transient field of a baffled planar piston having an arbitrary vibration amplitude distribution, J. Acoust. Soc. Am. 70 (1981) 186–204.
[12] J.N. Tjotta, S. Tjotta, Nearfield and farfield of pulsed acoustic radiators, J. Acoust. Soc. Am. 71 (1982) 824–834.
[13] H. Lasota, R. Salamon, B. Delannoy, Acoustic diffraction analysis by the impulse response method a line impulse response approach, J. Acoust. Soc. Am. 76 (1984) 280–290.
[14] G. Scarano, N. Denisenko, M. Matteucci, M. Pappalardo, A new approach to the derivation of the impulse response of a rectangular piston, J. Acoust. Soc. Am. 78 (1978) 1109–1113.
[15] C. Lee, P.J. Benkeser, A computationally efficient method for the calculation of the transient field of acoustic radiators, J. Acoust. Soc. Am. 96 (1994) 545–551.
[16] P. Crombie, P.A.J. Bascom, R.S.C. Cobbold, Calculating the pulsed response of linear arrays: accuracy versus computational efficiency, IEEE Trans. Ultrason. Ferroelect. Freq. Control 44 (1997) 997–1009.
[17] J.W. Goodman, Introduction to Fourier Optics, second ed., McGraw-Hill, New York, 1996.
[18] T. Kundu, Ultrasonic Nondestructive Evaluation: Engineering and Biological Material Characterization, CRC Press, Boca Raton, FL, 2004.
[19] D. Placko, T. Kundu, DPSM for Modeling Engineering Problems, Wiley-Interscience, Hoboken, NJ, 2007.
[20] T. Kundu, D. Placko, E. Kabiri Rahani, T. Yanagita, C. Minh Dao, Ultrasonic field modelling: a comparison between analytical, semi-analytical and numerical techniques, IEEE Trans. Ultrason. Ferroelect. Freq. Control, in press.
[21] J.A. Jensen, Linear Description of Ultrasound Imaging Systems, Notes for the International Summer School on Advanced Ultrasound Imaging, DTU, Technical Report, 1999.
[22] A.C. Kak, M. Slaney, Principle of Computerized Tomographic Imaging, IEEE Press, New York, 1987.
[23] J.Y. Lu, J. Cheng, J. Wang, High frame rate imaging system for limited diffraction array beam imaging with square-wave aperture weightings, IEEE Trans. Ultrason. Ferroelect. Freq. Control 53 (2006) 1796–1812.